ARTICLE IN PRESS [m5+;May 30, 2023;11:24]

FISEVIER

Available online at www.sciencedirect.com

ScienceDirect

Journal of Magnesium and Alloys xxx (xxxx) xxx



www.elsevier.com/locate/jma

Full Length Article

Assessment of a two-surface plasticity model for hexagonal materials

R. Vigneshwaran, A.A. Benzerga*

Department of Aerospace Engineering, Texas A&M University, College Station, TX 77843, USA
Received 23 December 2022; received in revised form 23 February 2023; accepted 19 April 2023
Available online xxx

Abstract

A computationally efficient two-surface plasticity model is assessed against crystal plasticity. Focus is laid on the mechanical behavior of magnesium alloys in the presence of ductility-limiting defects, such as voids. The two surfaces separately account for slip and twinning such that the constitutive formulation captures the evolving plastic anisotropy and evolving tension-compression asymmetry. For model identification, a procedure is proposed whereby the initial guess is based on a combination of experimental data and computationally intensive polycrystal calculations from the literature. In drawing direct comparisons with crystal plasticity, of which the proposed model constitutes a heuristically derived reduced-order model, the available crystal plasticity simulations are grouped in two datasets. A calibration set contains minimal data for both pristine and porous material subjected to one loading path. Then the two-surface model is assessed against a broader set of crystal plasticity simulations for voided unit cells under various stress states and two loading orientations. The assessment also includes microstructure evolution (rate of growth of porosity and void distortion). The ability of the two-surface model to capture essential features of crystal plasticity is analyzed along with an evaluation of computational cost. The prospects of using the model in guiding the development of physically sound damage models in Mg alloys are put forth in the context of high-throughput simulations.

© 2023 Chongqing University. Publishing services provided by Elsevier B.V. on behalf of KeAi Communications Co. Ltd.

This is an open access article under the CC BY-NC-ND license (http://creativecommons.org/licenses/by-nc-nd/4.0/)

Keywords: HCP metals; Plastic anisotropy; Reduced order model; Void growth; Void coalescence.

1. Introduction

Magnesium alloys are promising candidates for replacing conventional alloys in aerospace, automotive and defense applications. Magnesium alloys are highly anisotropic due to their hexagonal-close-packed crystalline structure. Their anisotropy manifests at various scales as it results from low crystal symmetry, strong crystallographic texture, and deformation twinning leading to tension-compression asymmetry. Thus, the plastic flow response is dependent upon orientation and loading mode.

Peer review under responsibility of Chongqing University

Much has been done in modeling the plastic flow of magnesium and its alloys using: (i) high-fidelity crystal plasticity [1–3]; (ii) viscoplastic self-consistent (VPSC) schemes [4,5];

E-mail address: benzerga@tamu.edu (A.A. Benzerga).

and (iii) phenomenological models [6]. In recent years, a subclass of the latter have emerged, which aim at capturing the essential features of crystal plasticity via some reduction in degrees of freedom in terms of the internal variables involved [7–9]. These are not directly derived from crystal plasticity by standard reduced-order modeling, e.g. Michel and Suquet [10], but they may be termed "heuristic reduced order models" of crystal plasticity. So far, the assessment of these models against crystal plasticity or experiments has been limited to relatively simple situations of macroscopically uniform deformation.

On the other hand, predicting damage progression to failure in Mg alloys (or HCP materials in general) requires coupled plasticity-damage models, a field in infancy [11]. To guide the development of damage models, it is paramount that reduced order models of damage-free plasticity be first assessed against, say crystal plasticity simulations that incorporate the key defects mediating ductile failure, namely voids.

https://doi.org/10.1016/j.jma.2023.04.013

2213-9567/© 2023 Chongqing University. Publishing services provided by Elsevier B.V. on behalf of KeAi Communications Co. Ltd. This is an open access article under the CC BY-NC-ND license (http://creativecommons.org/licenses/by-nc-nd/4.0/) Peer review under responsibility of Chongqing University

^{*} Corresponding author.

Unit cell analyses have recently been carried out on Mg alloys containing initial voids, spherical [12] or crack-like [13]. The analyses have revealed some aspects of plastic anisotropy that are captured by relatively simple porous material plasticity models [14] as well as crystallographic aspects that cannot be captured by these constitutive models. A first step towards developing physically sound but computationally tractable damage models is to investigate the capability of the heuristic reduced order models to reproduce crystal plasticity simulations of voided unit cells. This task is undertaken in this paper.

Here, a rate-dependent version [9] of a two-surface plasticity model [8] is used to carry out voided cell analyses. The corresponding constitutive relation has been assessed against unprecedented experiments in Kondori et al. [9]. Whether such assessment is sufficient is part of what this study set out to investigate. The results of unit cell calculations are thus compared against similar calculations using crystal plasticity, which were published in Selvarajou et al. [12]. The paper is organized as follows. Section 2 introduces the constitutive equations of the two-surface model and Section 3 the unit cell setup. Section 4 addresses parameter identification while Section 5 presents our critical assessment of the model. Finally, Section 6 discusses the computational efficiency of the model and alternative strategies for parameter identification.

2. Constitutive equations

2

Deformation of magnesium alloys is governed by two major deformation mechanisms: (i) dislocation glide (ii) twinning. The constitutive equations presented below, following [8,9], account for both mechanisms at a macroscopic scale. The total rate of deformation is additively decomposed as:

$$\mathbf{d} = \mathbf{d}^{e} + \mathbf{d}^{g} + \mathbf{d}^{t} \tag{1}$$

where the elastic part \mathbf{d}^e is given by isotropic hypoelasticity $\mathbf{d}^e = \mathbb{M} : \overset{\triangledown}{\sigma}$, the symbol \triangledown denoting the Jaumann rate, σ the Cauchy stress and \mathbb{M} the compliance tensor.

The plastic rate-of-deformations \mathbf{d}^g and \mathbf{d}^t are respectively obtained from plastic potentials Φ^g and Φ^t assuming normality, so that:

$$\mathbf{d}^{g} = \dot{\mathbf{p}}^{g} \frac{\partial \Phi^{g}}{\partial \sigma} \quad \text{and} \quad \mathbf{d}^{t} = \dot{\mathbf{p}}^{t} \frac{\partial \Phi^{t}}{\partial \sigma}$$
 (2)

where $\dot{p}^{\rm g}$, $\dot{p}^{\rm t}$ are plastic multipliers, shown to be rate measures of effective glide and twinning strain, and $\Phi^{\rm g}$, $\Phi^{\rm t}$ are expressed as:

$$\Phi^{g} = \bar{\sigma}^{g}(\sigma) - R^{g}(p^{g}, p^{t}) \tag{3}$$

$$\Phi^{t} = \bar{\sigma}^{t}(\boldsymbol{\sigma}) - R^{t}(p^{g}, p^{t}) \tag{4}$$

Here, $\bar{\sigma}^g$ and $\bar{\sigma}^t$ are homogeneous functions of degree 1 in σ . Also, R^g and R^t are the glide and twin strengths taken as functions of both effective strain measures p^g and p^t .

In a rate independent formulation, the plastic potentials have meaning of yield functions and the plastic multipliers \dot{p}^g , \dot{p}^t are determined by writing Kuhn–Tucker conditions for each surface. In the extended rate-dependent formulation, on the other hand, the effective strain rates are obtained from a Norton law:

$$\dot{p}^{i} = \dot{\epsilon}_{0}^{i} \left(\frac{\bar{\sigma}^{i}}{R^{i}}\right)^{n^{i}} \quad i = \begin{cases} g \text{ (glide)} \\ t \text{ (twinning)} \end{cases}$$
 (5)

where \dot{e}_{0}^{i} is a reference strain rate and n^{i} is a strain rate sensitivity parameter. The rate-insensitive limit is approached for $n^{i} \rightarrow \infty$. The present formulation may be extended to kinematic hardening by replacing the above defined effective stresses with driving stresses. In particular, a back-stress formulation would be appropriate for twinning under non-monotonic loading.

2.1. Deformation by dislocation glide

Slip-induced plasticity in Mg is strongly anisotropic. Following a classical approach, a transformed stress deviator is defined as

$$\mathbf{s}^{\mathbf{g}} = \mathbb{L}^{\mathbf{g}} : \boldsymbol{\sigma} \tag{6}$$

with \mathbb{L}^g being a fourth order tensor describing the anisotropy of yield strength due to slip. Here, \mathbb{L}^g has the following structure (using Voigt's notation and principal directions L, T, S)

$$\begin{pmatrix} \frac{1}{3} (l_{\text{TT}}^g + l_{\text{SS}}^g) & -\frac{1}{3} l_{\text{SS}}^g & -\frac{1}{3} l_{\text{TT}}^g & 0 & 0 & 0 \\ -\frac{1}{3} l_{\text{SS}}^g & \frac{1}{3} (l_{\text{SS}}^g + l_{\text{LL}}^g) & -\frac{1}{3} l_{\text{LL}}^g & 0 & 0 & 0 \\ -\frac{1}{3} l_{\text{TT}}^g & -\frac{1}{3} l_{\text{LL}}^g & \frac{1}{3} (l_{\text{LL}}^g + l_{\text{TT}}^g) & 0 & 0 & 0 \\ 0 & 0 & 0 & l_{\text{LT}}^g & 0 & 0 \\ 0 & 0 & 0 & 0 & l_{\text{TS}}^g & 0 \\ 0 & 0 & 0 & 0 & 0 & l_{\text{SL}}^g \end{pmatrix}$$

If s_i^g denote the eigenvalues of \mathbf{s}^g then the effective stress for glide $\bar{\sigma}^g$ in Eq. (3) is written as

$$\bar{\sigma}^{g} = \left[\frac{1}{2}\left(|s_{1}^{g} - s_{2}^{g}|^{a^{g}} + |s_{2}^{g} - s_{3}^{g}|^{a^{g}} + |s_{3}^{g} - s_{1}^{g}|^{a^{g}}\right)\right]^{1/a^{g}}$$
(8)

with a^g an exponent that controls the shape of the yield surface. The choices defined by Eqs. (7) and (8) are a reformulation of the non-quadratic yield model of Barlat et al. [15].

2.2. Deformation by twinning

Plastic deformation due to twinning introduces a strength differential effect. As above, a transformed stress deviator is defined as:

$$\mathbf{s}^{\mathsf{t}} = \mathbb{L}^{\mathsf{t}} : \mathbb{J} : \boldsymbol{\sigma} \tag{9}$$

where \mathbb{J} is the deviatoric projector and \mathbb{L}^t a fourth-order tensor the components of which read in Voigt's notation:

$$\begin{pmatrix} l_{LL}^{t} & \mathcal{L}_{LT}^{t} & \mathcal{L}_{LS}^{t} & 0 & 0 & 0 \\ \mathcal{L}_{LT}^{t} & l_{TT}^{t} & \mathcal{L}_{TS}^{t} & 0 & 0 & 0 \\ \mathcal{L}_{LS}^{t} & \ell_{TS}^{t} & \ell_{SS}^{t} & 0 & 0 & 0 \\ 0 & 0 & 0 & l_{LT}^{t} & 0 & 0 \\ 0 & 0 & 0 & 0 & l_{TS}^{t} & 0 \\ 0 & 0 & 0 & 0 & 0 & l_{SL}^{t} \end{pmatrix}$$

$$(10)$$

With s_i^t denoting the eigenvalues of \mathbf{s}^t , the effective stress for twinning $\bar{\sigma}^t$ that enters Eq. (4) is given by:

$$\bar{\sigma}^{t} = \left[\left(|s_{1}^{t}| - ks_{1}^{t} \right)^{a^{t}} + \left(|s_{2}^{t}| - ks_{2}^{t} \right)^{a^{t}} + \left(|s_{3}^{t}| - ks_{3}^{t} \right)^{a^{t}} \right]^{1/a^{t}}$$
 (11)

where a^t controls the shape of the yield surface, and the parameter k (-1 < k < 1) accounts for the *initial* strength differential effect. For k > 0, the yield stress is larger in tension than in compression and the coefficients of \mathbb{L}^t are all positive [8].

The choices defined by Eqs. (10) and (11) are a reformulation of the non-quadratic yield model of Cazacu et al. [6]. Note that their model has been extensively used for HCP alloys, in general, and Mg alloys, in particular. However, the two-surface formulation used here is essential for capturing proper evolution of plastic anisotropy, including the evolution of the net tension–compression asymmetry. In [6] the tension-compression asymmetry is fixed, which is inconsistent with experimental data.

2.3. Strain hardening

The flow strengths of individual mechanisms, R^g and R^t entering Eqs. (3) and (4), are taken as a combination of Voce-like laws for self hardening and linear laws for latent hardening:

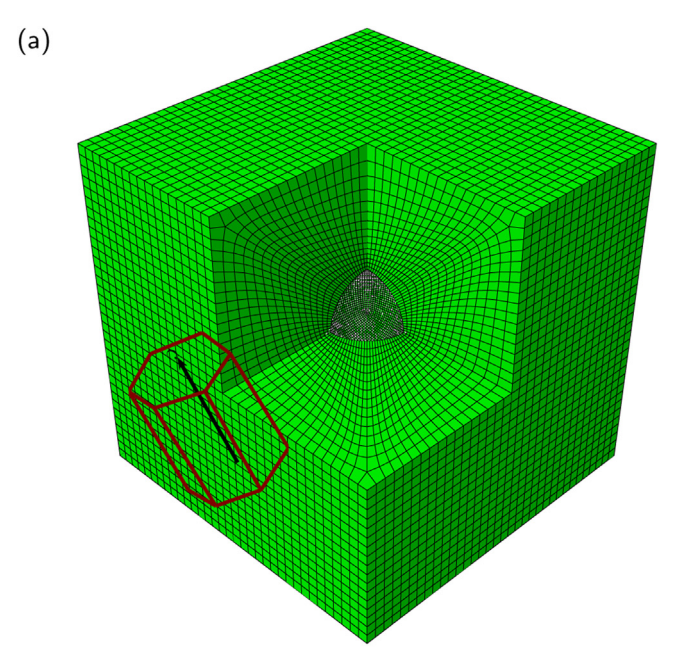
$$R^{g} = R_{0}^{g} + Q^{g}(1 - \exp(-b^{g}p^{g})) + \mathcal{H}^{tg}p^{t}$$
(12)

$$R^{t} = R_{0}^{t} + Q^{t}(\exp(b^{t}p^{t}) - 1) + H^{t}p^{t} + \mathcal{H}^{gt}p^{g}$$
(13)

Thus, four parameters $(R_0^g, Q^g, b^g, \mathcal{H}^{tg})$ enter hardening by glide and five parameters $(R_0^t, Q^t, b^t, H^t, \mathcal{H}^{gt})$ enter hardening by twinning.

3. Unit cell calculations

Three-dimensional (3D) calculations of unit cells containing a central spherical void were carried out, Fig. 1(a). Plastic flow in the matrix was described using the constitutive relation of Section 2, which was implemented as a user material subroutine (UMAT) in the commercial finite element code ABAQUS.



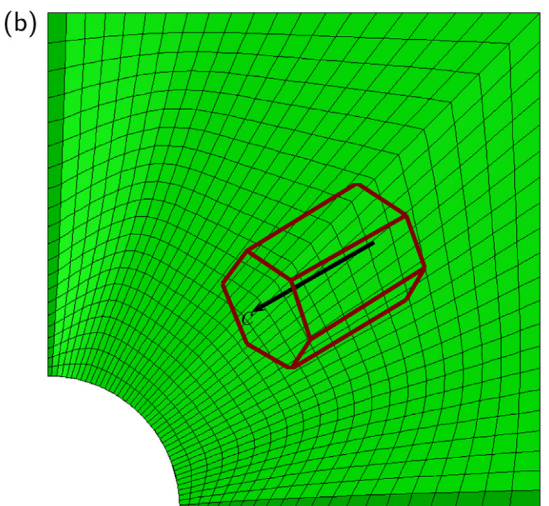


Fig. 1. (a) Full 3D unit cell embedding a spherical void. (b) Axisymmetric unit cell used in the optimization procedure.

Macroscopic measures of stress and strain rate are defined as volume averages of their microscopic counterparts:

$$\Sigma = \frac{1}{V} \int_{V} \boldsymbol{\sigma} \, dV, \qquad \mathbf{D} = \frac{1}{\mathbf{V}} \int_{V} \mathbf{d} \, dV. \tag{14}$$

In a given calculation, the unit cell is subjected to proportional stressing. Thus, the overall stress triaxiality ratio, T, and the Lode parameter, L, are kept fixed throughout the loading history. Not only do such loading conditions aid in analysis but also in making contact with similar calculations using crystal plasticity for the matrix behavior [12]. The dimensionless stress state parameters are defined as: $T = \Sigma_{\rm eq}/\Sigma_{\rm m}$ and $L = (2\Sigma_2 - \Sigma_1 - \Sigma_3)/(\Sigma_3 - \Sigma_1)$ where $\Sigma_{\rm eq}$ and $\Sigma_{\rm m}$ are the equivalent and mean normal stresses,

respectively:

$$\Sigma_{\text{eq}} = \sqrt{\frac{3}{2}\Sigma' : \Sigma'} \quad \Sigma_{\text{m}} = \frac{1}{3}\text{tr }\Sigma$$
 (15)

the prime standing for the deviator, and the Σ_i 's denote principal stresses ($\Sigma_1 \leq \Sigma_2 \leq \Sigma_3$).

Periodic boundary conditions were imposed. To achieve constant T and L load paths, the algorithm proposed by Zhu et al. [16] was employed using a custom coded multipoint constraint (MPC) subroutine in ABAQUS, the details of which are given elsewhere.

Here, only axisymmetric stress states are considered with $\Sigma_1 = \Sigma_2$. Thus, $\Sigma_{\rm eq} = \Sigma_3 - \Sigma_1$, L = -1 and T may vary from one calculation to another. The calculations still need to be 3D because of matrix anisotropy. To simplify parameter calibration, however, auxiliary two-dimensional axisymmetric calculations were also carried out, Fig. 1(b). Such calculations are similar in their principle to those of Koplik and Needleman [17], also used in subsequent work on anisotropic matrices [14,18].

Each calculation was post-processed in such a way that the void dimensions and volume are output at every time step. The void volume fraction (or porosity f) is calculated from the total volume of sound material and the current dimensions of the cell as in Koplik and Needleman [17]. This is exact, up to numerical errors. The void dimensions are approximately evaluated assuming an ellipsoidal shape with semi-axes a, b, c, with a along the semi major axis of the void. To this end, the URDFIL subroutine of Abaqus was used, which enabled real-time tracking of the void during deformation.

A monotonically increasing strain measure $E_{\rm eq}$ is used to plot overall stress-strain responses as well as porosity versus strain evolution:

$$E_{\text{eq}} = \frac{2}{3}(E_3 - E_1), \qquad E_i = \ln(l_i/L_i)$$
 (16)

where l_i and L_i denote the current and initial dimensions of the cell in the x_i direction.

In the 3D and 2D calculations, linear C3D8 and CAX4 elements were used. In Fig. 1 the number of elements is about 40,000 and 400, respectively, but a coarser mesh was used in the optimization with 200 elements.

In addition to the cell model calculations, material point simulations were also used for calibration. These consist of a single element calculation in simple tension using an eightnoded brick element with reduced integration (C3D8R). The loading direction is either L, which represents the prismatic loading orientation in Selvarajou et al. [12], or S, which represents the c-axis orientation in Selvarajou et al. [12]. The equivalent stress and strain measures for the material point simulations are respectively denoted by $\sigma_{\rm eq}$ and p, where $p = p^{\rm g} + p^{\rm t}$.

4. Comparison with crystal plasticity

4.1. Benchmark simulations

The crystal plasticity calculations of Selvarajou et al. [12] serve as the main benchmark. These authors carried out unit cell calculations similar to those described above, but using a crystal plasticity constitutive relation for HCP metals. Table 1 summarizes the eight cases they considered: four triaxiality values per loading orientation (prismatic or c-axis loading). In addition, uniaxial responses in simple tension (T=1/3) were simulated in Selvarajou et al. [12], which are referred to as "material point" simulations in the table.

Under overall uniaxial loading (T=1/3) it is important to distinguish between the material point calculations for the pristine (void-free) material and the cell model with a void. The stress, strain and strain-rate states are uniform in the former, but not in the latter. For example, Selvarajou et al. [12] showed evidence of a void-induced hardening, resulting in a higher flow stress than with the pristine material for c-axis loading. This is due to the activation of more deformation systems around the void than would be expected on the mere basis of the overall stress state (which is uniaxial).

Output data provided in Selvarajou et al. [12] includes overall stress–strain responses ($\Sigma_{\rm eq}$ versus $E_{\rm eq}$ using the above definitions) as well as the evolution of porosity and main void axes. This is the only data that will be used in making comparisons with the heuristic reduced order model (ROM) of Section 2. Any details beyond that (e.g. microscopic fields) go beyond what is expected of a ROM.

The crystal plasticity simulations in Selvarajou et al. [12] are divided into two datasets: a calibration dataset (identified by (c) in Table 1) and an assessment dataset. The calibration dataset contains the minimum set of data needed for robust calibration. Note that the calibration data only includes stress-strain curves so that porosity versus strain data in the so-called calibration set is exclusively used for assessment, not for calibration of the ROM.

4.2. Parameters of the ROM

The crystal plasticity model and heuristic ROM do not have the same elasticity parameters. Young's modulus E is obtained from the average initial slopes of the pure Mg single crystal stress-strain responses in Selvarajou et al. [12] under prismatic and c-axis loading. The value of Poisson's ratio ν is obtained from the literature for pure Mg. In addition to these, the ROM involves the following parameters, given in their order of appearance in Section 2.

- 1. The four (4) rate-sensitivity parameters, $\dot{\epsilon}_0^i$ and n^i entering Eq. (5) (two per mode of deformation, glide versus twinning).
- 2. The six glide anisotropy coefficients (l_{XY}^g) in Eq. (7) (of which only five (5) are independent) and the exponent a^g in Eq. (8).

- 3. The nine twinning anisotropy coefficients (l_{XY}^t and \mathcal{L}_{XY}^t) in Eq. (10) (of which only eight (8) are independent), the exponent a^t and the stress differential parameter k in Eq. (11).
- 4. The four (4) glide hardening parameters (R_0^g , Q^g , b^g , \mathcal{H}^{tg}) in Eq. (12) and five (5) twinning hardening parameters (R_0^t , Q^t , b^t , H^t , \mathcal{H}^{gt}) in Eq. (13).

Therefore, there are 29 independent parameters in total entering the constitutive formulation.

4.3. Simplification

Since the anisotropy parameters are defined up to a multiplicative constant, we take $l_{\rm LL}^{\rm g}=1$, $l_{\rm LL}^{\rm t}=1$ with no loss of generality. Following Kondori et al. [9], we also take $a^{\rm g}=a^{\rm t}=4$. Furthermore, using some observations made by Selvarajou et al. [12] the hardening in glide due to twinning deformation is not well distinguished in their material. There is no case where deformation enters into the twinning-affected regime after a glide-dominated one. Also, the self-hardening in twinning is approximately linear. Hence the exponential function is avoided. We then simplify the hardening forms by taking $\mathcal{H}^{\rm tg}=0$ in Eq. (12) and $Q^{\rm t}=0$, $b^{\rm t}=1$ in Eq. (13). Thus, only six hardening parameters are retained.

Next, the Norton constants are taken to be the same for glide and twinning, just like in the CP calculations in Selvarajou et al. [12]. Furthermore, their values in Selvarajou et al. [12] are adopted here.

This leaves a total of 20 parameters to be identified. The goal is to identify these parameters from a minimal crystal plasticity simulation dataset, Table 1. For reference, there are about 26 (free) parameters in the crystal plasticity formulation employed by Selvarajou et al. [12].

4.4. Optimization strategy

An iterative procedure was followed for calibrating the ROM of Section 2 using the benchmark crystal plasticity simulations in Selvarajou et al. [12]. The procedure is schematically shown in Fig. 2.

Once a set of initial parameters is chosen, four finite element simulations (two voided unit cells and two material point calculations) are carried out for the conditions identified with a (c) in Table 1. The "distance", in terms of an error norm, between the ROM and CP simulations is evaluated using a cost function, and a new set of parameters is determined using a Nelder–Mead optimization algorithm of the Z-set package [19]. This process is repeated until the cost function reaches a minimum value or further minimization is impossible.

The cost function, \mathcal{E} , is entirely based on the stress–strain responses, as noted above. For the cell model results, an essential feature is the abrupt stress drop corresponding to the onset of coalescence, which represents a measure of strain to failure. In order to give that measure a larger weight, we

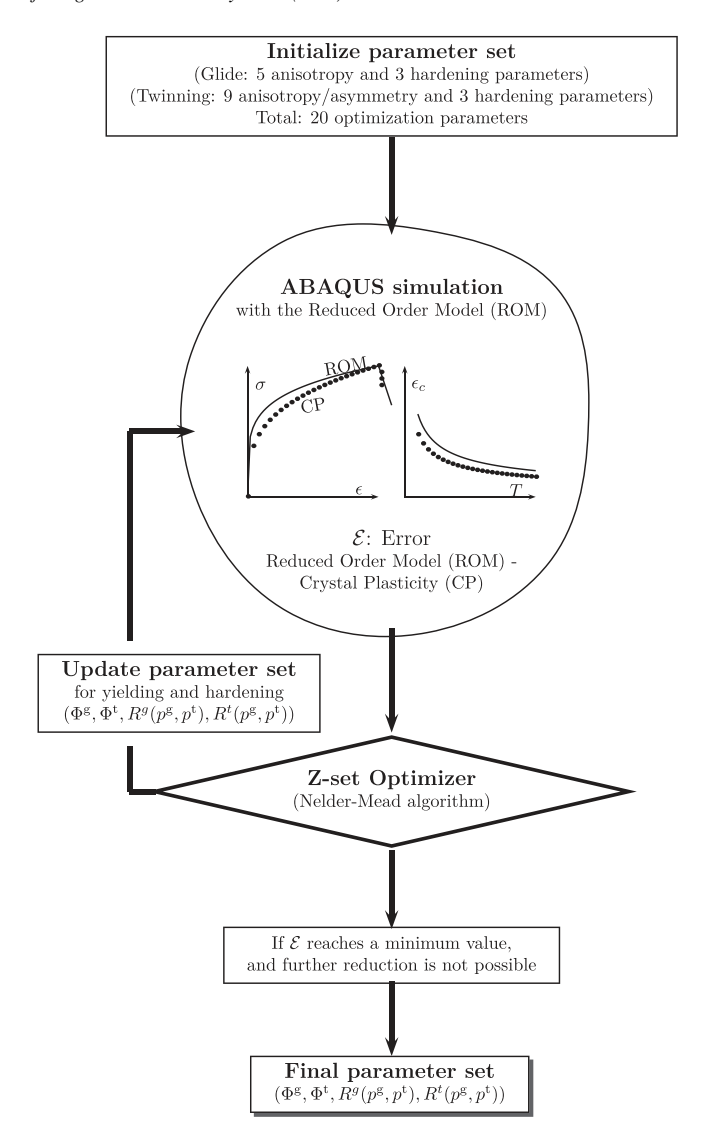


Fig. 2. Iterative procedure used for model calibration.

define the cost function as follows:

$$\mathcal{E} = \sum_{I=1}^{N} E^{I} \tag{17}$$

where N denotes the number of test simulations, i.e. elements in the calibration set (here 4) and

$$E^{I} = \frac{w_{\sigma}^{I}}{\epsilon_{\text{max}}^{I}} \int_{0}^{\epsilon_{\text{max}}^{I}} \left(\sigma_{\text{CP}}^{I} - \sigma_{\text{ROM}}^{I}\right)^{2} d\epsilon + \frac{w_{\epsilon}^{I}}{2} \left(\epsilon_{\text{CP}c}^{I} - \epsilon_{\text{ROM}c}^{I}\right)^{2}$$
(18)

For a given test I, E^I quantifies the difference between the ROM and CP simulations in terms of the stress-strain curve and the strain to failure in the cell model. More specifically, w_{σ}^{I} , w_{ϵ}^{I} are weights, ϵ_{\max}^{I} is the total strain reached in a given simulation I, σ_{CP}^{I} , σ_{ROM}^{I} denote appropriate equivalent stresses, and $\epsilon_{\text{CP}c}^{I}$, $\epsilon_{\text{ROM}c}^{I}$ are the strains to failure (available only for cell simulations). The strain to failure is given a

6

Datasets from Selvarajou et al. [12]'s crystal plasticity (CP) benchmark simulations. Data marked with (c) was used for calibration.

Dataset	T	Loading	Simulation type
1 (c)	1/3	Prismatic	Material Point
2 (c)	1/3	c-axis	Material Point
3	1/3	Prismatic	Cell Model
4 (c)	1	Prismatic	Cell Model
5	2	Prismatic	Cell Model
6	3	Prismatic	Cell Model
7	1/3	c-axis	Cell Model
8 (c)	1	c-axis	Cell Model
9	2	c-axis	Cell Model
10	3	c-axis	Cell Model

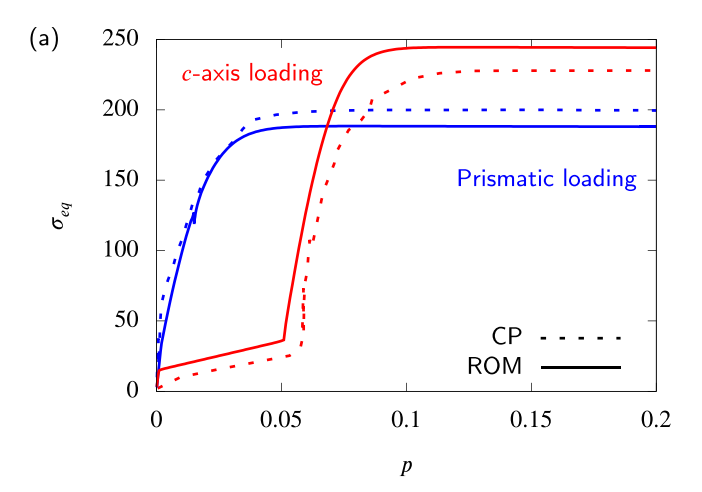
bigger weight where relevant. Hence, we take $w_{\sigma}^{I}=1$ but $w_{\epsilon}^{I}=o(100)$, for all I.

To reduce computational cost, the axisymmetric 2D unit cell model calculations were used for optimization of the parameters. After convergence, 3D cell calculations were carried out using the optimized parameters for purposes of model assessment.

Finally, a word on initialization. The Nelder-Mead algorithm was chosen compared to other optimization algorithms available in Z-set, such as the Levernberg-Marquardt or sequential quadratic programming (SQP) algorithms, as it is reasonably more robust to variations in initial conditions. Here, the initial set of parameters was determined in two steps. First, the parameters introduced by Kondori et al. [9] were employed. Since these were fit on experiments on a Mg alloy they were not particularly well suited for comparison with the crystal plasticity simulations in Selvarajou et al. [12]. Therefore, in a second step a recent set of large-scale polycrystal simulations by Indurkar et al. [20] were used. Their polycrystal stress-strain curves were used as input to an optimization scheme as above. Details of this step are provided in Appendix. This initialization step has no major consequence on the message of the paper. However, it provides a reasonable initialization step when such data is available.

5. Results

The optimized ROM material parameters are listed in Table 2. As expected, the initial strength of the twinning mode, $R_0^t = 17.4$ MPa is lower than that for the glide mode $R_0^g = 72$ MPa. Depending on the loading direction and the stress differential parameter (here k = 0.57), the activation of twinning deformation is determined by the dominant potential, Eqs. (3) and (4). The large value of the latent hardening term \mathcal{H}^{gt} illustrates that as soon as a small glide deformation occurs, twin strength increases drastically, and the deformation transitions into a glide mode. The glide anisotropy coefficients vary between 1.72 and 2.13; compare with the range 1.09 to 1.69 for AZ31B in Kondori et al. [9]. The twinning anisotropy coefficients vary between 0.43 and 2.47; compare with the range 0.22 to 0.97 in Kondori et al. [9]. As expected, the anisotropy of a single crystal is stronger



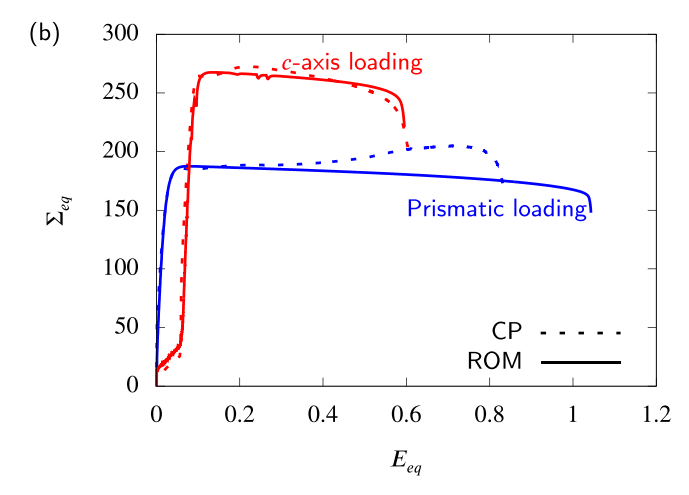


Fig. 3. Best fit of the ROM (this paper) on crystal plasticity (CP) simulations in Selvarajou et al. [12] for two loading orientations; see data labeled (c) in Table 1. (a) Effective stress, $\sigma_{\rm eq}$, versus effective strain, p, for uniaxial tension of pristine material. (b) Cell equivalent stress, $\Sigma_{\rm eq}$, versus equivalent strain, $E_{\rm eq}$, for voided cell with initial porosity $f_0=1\%$ and T=1.

than that of a polycrystal with a basal texture. The fact that $l_{\text{TT}}^{\text{g}} \approx l_{\text{SS}}^{\text{g}}$ is a consequence of using axisymmetric elements in the calibration process. The consequences this may have in predicting the anisotropic evolution of microstructure will be discussed.

5.1. ROM-CP comparison

Figure. 3 evaluates the quality of the fit using the optimized ROM parameters against the calibration dataset from crystal plasticity, Table 1. Uniaxial tension responses of the pristine Mg material are shown in Fig. 3(a). The voided cell model responses are shown in Fig. 3(b) for T=1 under prismatic and c-axis loading. The dashed lines correspond to the CP reference simulations and the solid lines correspond to ROM calculations. At least one triaxial tension data on the cell model and uniaxial tension data on pristine material are required for the ROM to capture the void-induced hardening as well as strain to coalescence observed in CP simulations. The following observations are in order.

Table 2
Optimized material parameters. Stress-like parameters are expressed in MPa. The number of parameters for each group is indicated in parentheses. Parameters marked with an asterisk were fixed in the optimization process.

Elasticity	Isotropy (2)	E	ν									
		15000.0*	0.29*									
Viscoplasticity	Norton's law (2)	$\dot{\epsilon}_0$	n									
		0.001*	50.0*									
Glide	Hardening (4)	R_0^{g}	Q^{g}	b^{g}	\mathcal{H}^{tg}							
		72.0	332.0	268.0	0.0^{*}							
	Anisotropy (7)	$l_{ m LL}^{ m g}$	$l_{\mathrm{TT}}^{\mathrm{g}}$	$l_{\mathrm{SS}}^{\mathrm{g}}$	$l_{ m LT}^{ m g}$	$l_{\mathrm{TS}}^{\mathrm{g}}$	$l_{ m SL}^{ m g}$	a^{g}				
		1.0*	2.13	2.08	1.95	1.82	1.72	4.0^{*}				
Twinning	Hardening (5)	$R_0^{\rm t}$	Q^{t}	b^{t}	H^{t}	$\mathcal{H}^{ ext{gt}}$						
		17.4	0.0^{*}	1.0*	571.0	1.1×10^{7}						
	Anisotropy (11)	$l_{ m LL}^{ m t}$	$l_{\mathrm{TT}}^{\mathrm{t}}$	$l_{\mathrm{SS}}^{\mathrm{t}}$	$l_{ m LT}^{ m t}$	$l_{ m TS}^{ m t}$	$l_{ m SL}^{ m t}$	$\mathcal{L}_{ ext{LT}}^{ ext{t}}$	$\mathcal{L}_{ ext{TS}}^{ ext{t}}$	$\mathcal{L}_{\mathrm{SL}}^{\mathrm{t}}$	a^{t}	k
		1.0*	2.47	0.52	0.43	1.0	1.07	1.79	1.56	1.68	4.0*	0.57

- For the pristine material, unlike with standard J_2 plasticity, the crystal plasticity material exhibits an orientation-dependent macroscopic stress-strain response. The results presented in Fig. 3(a) show the extent of the differences.
 - Under *c-axis loading*, deformation occurs by twinning, resulting in a softer response initially, see Fig. 3(a). The material linearly hardens in the twinning-affected regime. Then, as in CP, the deformation by glide becomes dominant at a strain of about 5%, and the effect of latent hardening gradually deactivates the twinning deformation, while the flow stress increases. Eventually, the flow stress saturates at a value higher than for the prismatic loading case after 10% of strain.
 - Under *prismatic loading*, deformation by dislocation glide occurs first, as in the crystal plasticity simulation, resulting in a hard initial response, see Fig. 3(a). The Voce-type hardening law captures stress saturation after 5% of strain.

The ROM captures the essential features of the CP simulations. That the ROM is capable of capturing such effects has already been established in Kondori et al. [9]. The errors are larger in Fig. 3(a) than in Kondori et al. [9] because of the additional constraint of satisfying void growth and coalescence simulations in Fig. 3(b).

- For the voided material, the macroscopic stress-strain responses show a trend similar to the pristine material. However, the presence of a void introduces a competition between softening due to void growth, and void-induced hardening.
 - Under *c-axis loading*, the deformation due to twinning occurs first, resulting in a soft initial response that eventually transitions into the glide mode, see Fig. 3(b). Regions of tension and compression around the void undergo different deformation mechanisms due to the stress differential effect. This effect is more pronounced under *c*-axis loading; hence a harder response is obtained with higher flow stress levels, at least for low to moderate triaxialities (T=1/3,1), in comparison with the pristine case. The stress drop obtained at $E_{eq}\sim 0.6$ is due to the onset of void coalescence (see Benzerga [21] for background).

• Under *prismatic loading*, the deformation by glide occurs first, resulting in a hard initial response, see Fig. 3(b). Then, the porosity grows leading to softening, and the load drops because of coalescence. The load drop occurs at $E_{\rm eq} \sim 0.85$ and $E_{\rm eq} \sim 1.0$ for the CP and ROM simulations, respectively.

The ROM captures the macroscopic stress-strain response, the void-induced hardening and the softening due to porosity growth under c-axis loading. However, under prismatic loading, the secondary hardening at $E_{\rm eq} \sim 0.6$ and the strain to coalescence are not captured well.

5.2. Model assessment

By model assessment we mean (i) conducting a series of comparisons for loading cases not used for calibration and (ii) porosity growth predictions for the loading cases used for calibration (recall that porosity versus strain curves were not used as input to the optimizer.)

Figure 4 shows the porosity, f, versus strain, $E_{\rm eq}$, curves corresponding to the cell model responses shown in Fig. 3(b). There is a tendency for the 2D ROM simulations to some-

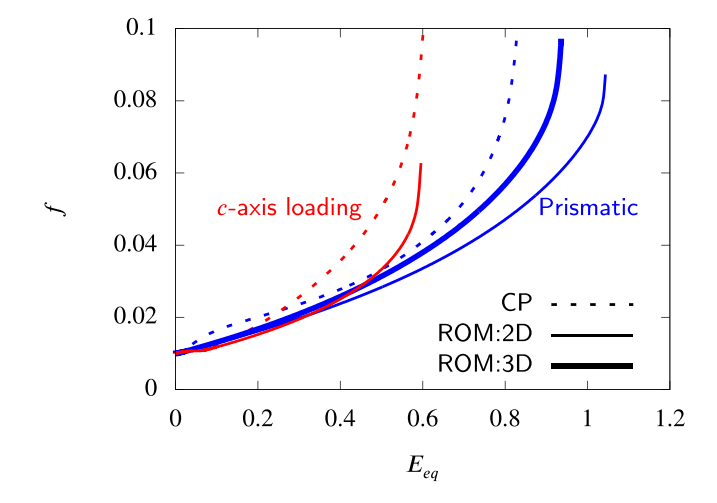


Fig. 4. Porosity, f, versus cell equivalent strain, $E_{\rm eq}$, for voided cell with initial porosity $f_0=1\%$ and T=1, corresponding to the responses in Fig. 3(b). The 3D cell response for prismatic loading is also shown for comparison.

R. Vigneshwaran and A.A. Benzerga/Journal of Magnesium and Alloys xxx (xxxx) xxx

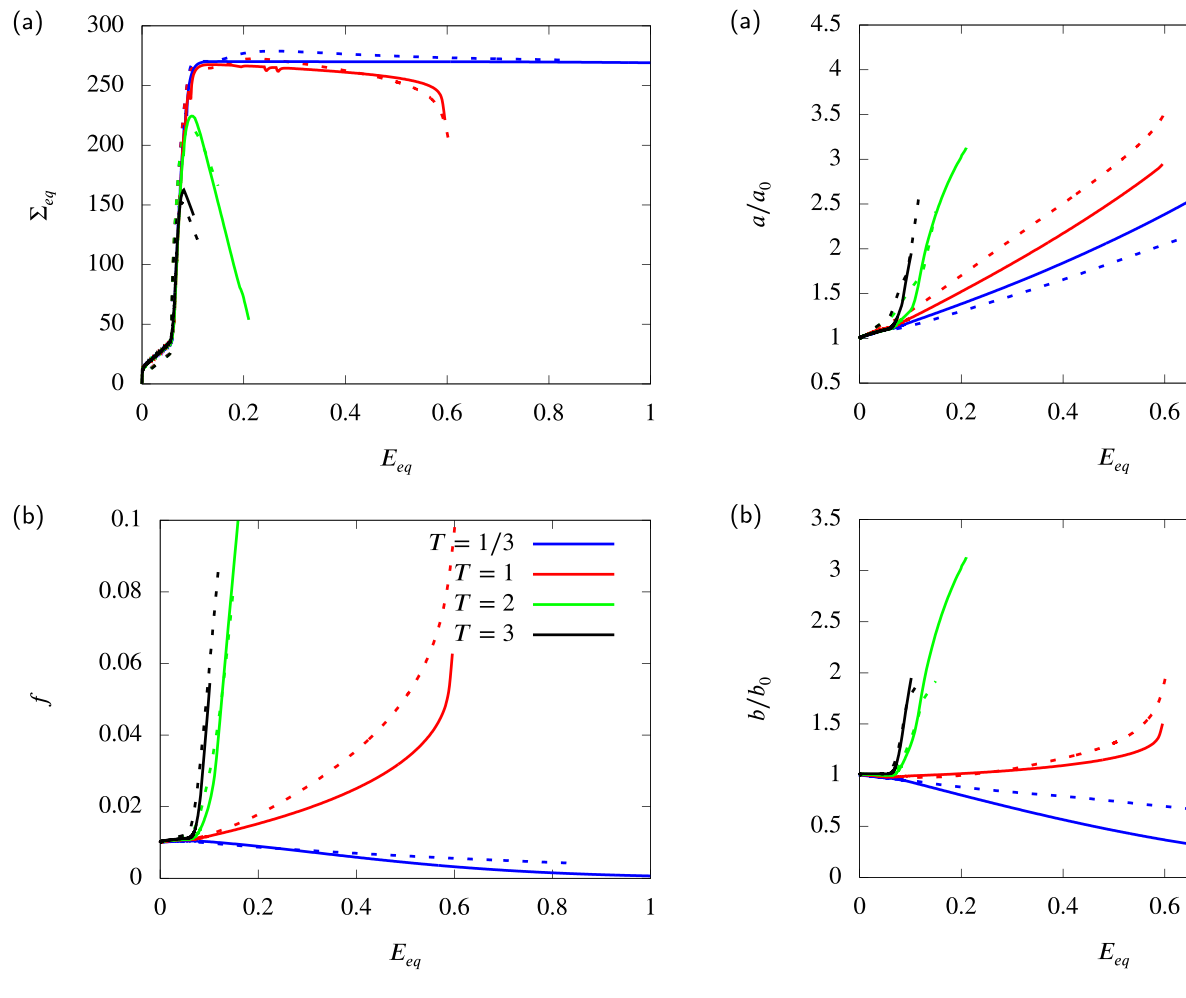


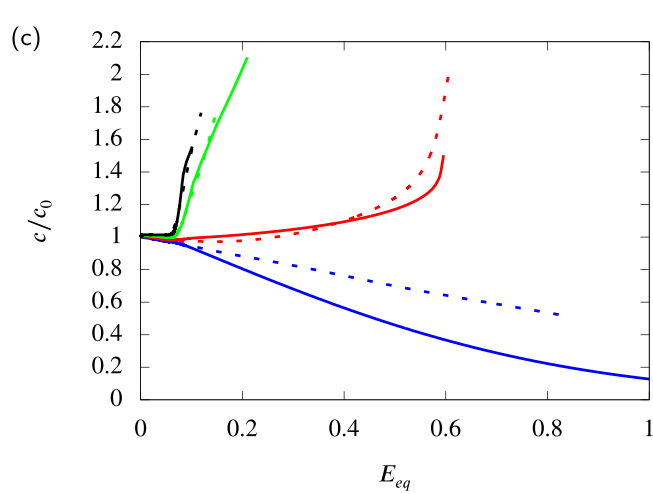
Fig. 5. (a) Cell equivalent stress, $\Sigma_{\rm eq}$, (b) Porosity, f, versus cell equivalent strain, $E_{\rm eq}$, for voided cell with initial porosity $f_0=1\%$ under c-axis loading for T=1/3,1,2,3. The dashed lines correspond to CP simulations in Selvarajou et al. [12], and the solid lines correspond to ROM simulation.

what underestimate the rate of porosity growth. However, keeping in mind that void growth results from microscopic plastic flow in the matrix and that microscopic fields are beyond what is expected of a ROM by definition, overall the porosity evolution predictions are quite good. Note in passing the significant improvement in the prismatic case when using full 3D simulations. The c-axis simulations are not very dependent on dimensional order because the response is quasitransversely isotropic in that case. In what follows, therefore, 3D simulation results are only shown for the prismatic orientation.

5.2.1. c-axis loading

8

Figure 5 shows cell model curves of equivalent stress, $\Sigma_{\rm eq}$, versus equivalent strain, $E_{\rm eq}$, and corresponding curves of porosity, f, versus $E_{\rm eq}$ for four values of the stress triaxiality ratio T. The benchmark crystal plasticity results are plotted dashed whereas the ROM predictions are shown with solid lines. Figure 6 shows the corresponding evolution of the void's semi-axes, normalized by their initial values, a_0 ,



0.8

0.8

1

1

Fig. 6. The major, a, intermediate, b, and minor, c, semi axes of the void, versus cell equivalent strain, $E_{\rm eq}$, for voided cell with initial porosity $f_0=1\%$ under c-axis loading for T=1/3,1,2,3. The dashed lines correspond to CP simulations in Selvarajou et al. [12], and the solid lines correspond to ROM simulation.

 b_0 , c_0 . Recall that the T=1 case (shown red; color online) was used for calibration. Key features are as follows.

• The sigmoidal character of the stress-strain response of the pristine material (Fig. 3(a)) affects all macroscopic

(

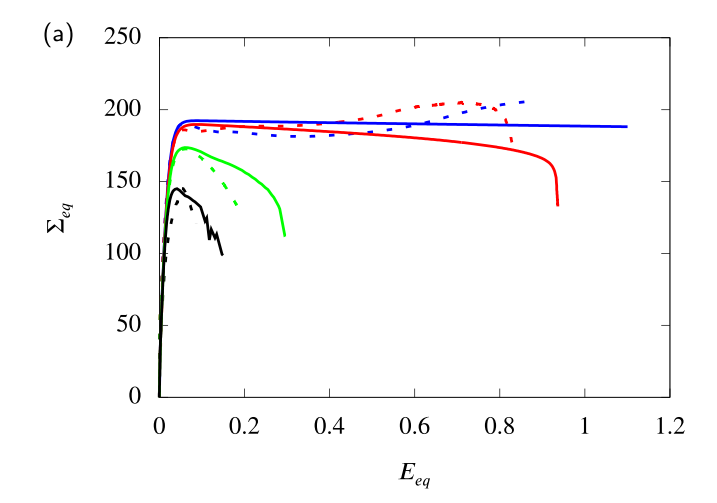
stress-strain responses in Fig. 5(a), irrespective of triaxiality. However, except for T=1/3, the effective responses now have a softening component, which is porosity induced. The higher the triaxiality the more severe the softening. Given that the hardening capacity is low after twinning is complete, the material behaves as nearly perfectly plastic. It is known, under such circumstances, that the porosity induced softening may take effect immediately as the cell transitions to a uniaxial deformation mode corresponding to accelerated void growth after the onset of void coalescence [17]. This is the case for T=2 and T=3.

- It is remarkable that the ROM predictions in Fig. 5(a) reproduce extremely well the crystal plasticity results for the T=1/3, T=2 and T=3 cases, which were not used for calibration. The accurate predictions include the strain to failure, defined as above (i.e. onset of void coalescence).
- The evolution of porosity is also very well reproduced (Fig. 5(b)), especially in cases for which the stress-strain curves were not used in calibration. The higher the triaxiality the faster the void growth, as is well known [22].
- The evolution of the semi-axes of the void is also well reproduced at all triaxialities, Fig. 6. For T=1/3 the ROM predictions exaggerate the lateral void shrinkage. Overall, the predictions are remarkable given that the evolution of the semi-axes represents a deeper layer of detail in probing the ROM's performance.
- The case of overall uniaxial tension T = 1/3 merits special attention.
 - There is a void-induced hardening in this case, which was thoroughly discussed in Selvarajou et al. [12]. The effect is appreciated by noting that the flow stress in tension for the pristine material is below 250 MPa (from Fig. 3(a)). By way of contrast, in the voided material it is well above 250 MPa (see Fig. 5(a)) even if the void actually tends to close while elongating. In the crystal plasticity simulations, this effect results from activation of multiple deformation systems beyond the favorable extension twinning. Not only does the ROM predict the void-induced hardening (Fig. 5(a)) but also the corresponding porosity decrease (Fig. 5(b)).
 - In standard J_2 plasticity, the typical prediction for T = 1/3 is that the porosity saturates after a slight increase. Under c-axis loading there is actually a significant decrease, which is well captured by the ROM, Fig. 5(b).

5.2.2. Prismatic loading

Figure 7 shows cell model curves of $\Sigma_{\rm eq}$ versus $E_{\rm eq}$ and corresponding curves of porosity versus $E_{\rm eq}$ for four values of the triaxiality T. The crystal plasticity and ROM predictions are plotted using dashed and solid lines, respectively. In addition, Fig. 8 depicts the evolution of the void's semi-axes. Salient features are as follows.

• The overall stress-strain responses in Fig. 5(a) are dominated by glide from the outset of plastic flow. Unlike the



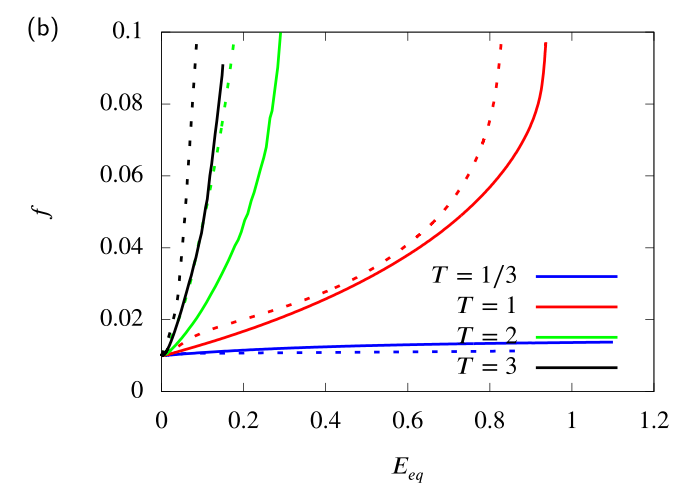
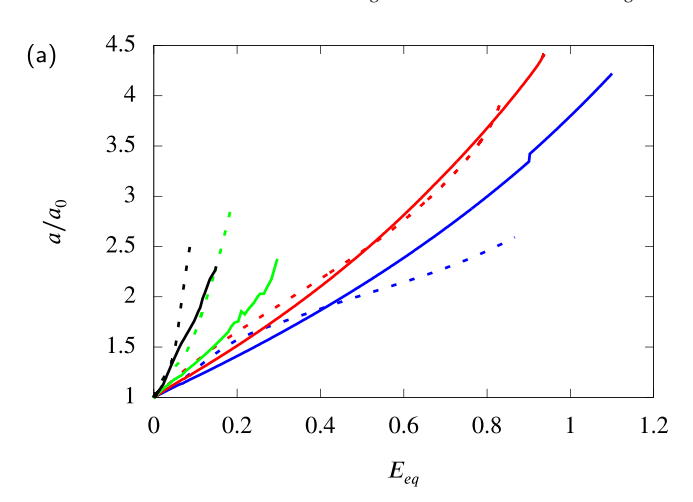


Fig. 7. (a) Cell equivalent stress, $\Sigma_{\rm eq}$, (b) Porosity, f, versus cell equivalent strain, $E_{\rm eq}$, for voided cell with initial porosity $f_0=1\%$ under prismatic loading for T=1/3,1,2,3. The dashed lines correspond to CP simulations in Selvarajou et al. [12], and the solid lines correspond to ROM simulation.

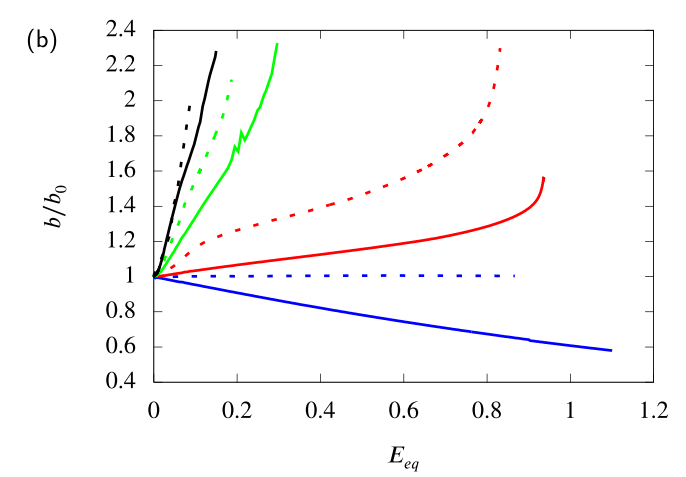
pristine material (Fig. 3) the voided cells exhibit softening after sufficient straining, except for T = 1/3. The softening is induced by porosity growth, Fig. 5(b).

- The correspondence between ROM and CP results is not as good as in Fig. 5 for c-axis loading. A main part of this is that the CP simulations exhibit some secondary hardening for T=1/3 and T=1 after $E_{\rm eq}\sim 0.6$, which the ROM does not capture. As a result, the ROM overestimates the softening at low triaxiality but underestimates it at high triaxiality.
- Correspondingly, the ROM underestimates the growth of porosity in all but the T=1/3 case. The relative error becomes important at high triaxiality. This point merits further discussion below.
- The evolution of the semi-axes of the void is predicted reasonably well, Fig. 8, with some discrepancies that are worth analyzing. Consider the T=1 case for which the stress-strain curve was used for ROM calibration. The main axis of the void, a, is predicted quite well, Fig. 8(a). However, the transverse axes, b and c, are not. In fact, the

R. Vigneshwaran and A.A. Benzerga/Journal of Magnesium and Alloys xxx (xxxx) xxx



10



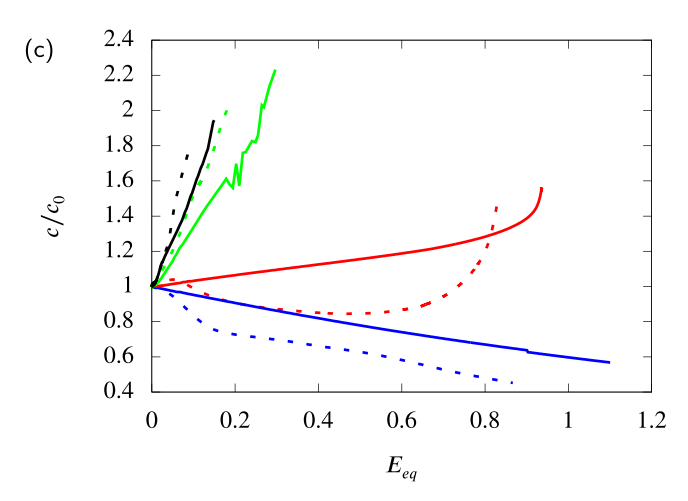


Fig. 8. The major, a, intermediate, b, and minor, c, semi axes of the void, versus cell equivalent strain, $E_{\rm eq}$, for voided cell with initial porosity $f_0=1\%$ under c-axis loading for T=1/3,1,2,3. The dashed lines correspond to CP simulations in Selvarajou et al. [12], and the solid lines correspond to ROM simulation.

ROM predicts similar evolution for b and c whereas the CP predictions show strong transverse anisotropy, Fig. 8(b) and (c). In other words, the initially spherical void develops into a fully 3D void. The reason for this is obviously

Table 3
The computational cost for each simulation using the reduced order model (ROM). The average time consumed for every simulation case and the number of CPUs considered are listed.

T Loading		Simulation type	CPUs	Time (s)
1/3	Prismatic	Material Point	1	30
1/3	c-axis	Material Point	1	30
1/3	Prismatic	2D Cell Model	15	200
1/3	c-axis	2D Cell Model	15	1100
1	Prismatic	2D Cell Model	15	800
1	c-axis	2D Cell Model	15	700
2	Prismatic	2D Cell Model	15	400
2	c-axis	2D Cell Model	15	700
3	Prismatic	2D Cell Model	15	400
3	c-axis	2D Cell Model	15	800
1/3	Prismatic	3D Cell Model	48	15,000
1	Prismatic	3D Cell Model	48	16,000
2	Prismatic	3D Cell Model	48	9000
3	Prismatic	3D Cell Model	48	8500

the use of 2D axisymmetric calculations during calibration. This led to $l_{\rm TT}^{\rm g} \approx l_{\rm SS}^{\rm g}$.

6. Discussion

6.1. Computational efficiency

Table 3 lists the computational time and number of CPUs used per calculation for all simulations with the reduced order model. The data is for the 2D, 3D cell simulations and 3D material point simulations; see Section 3. In the cell calculations, the CPU time is evaluated up to the onset of void coalescence, i.e. when the cell's deformation becomes suddenly uniaxial. When the latter does not occur (T=1/3) calculations are stopped at $E_{\rm eq}=1.1$. Where relevant, the listed times are averages over the many iterations taken during optimization of the parameters. Calculations that involve multiple deformation modes, typically the c-axis loading cases, require more iterations. The 3D calculations employed for prismatic loading require about 4.5 h with 48 CPUs for the T=1 case. The total cost of the 3D calculations (CPUs \times Time) is about 65 times their 2D counterparts.

Selvarajou et al. [12] did not report CPU times for their calculations. However, there is a good order of magnitude difference between the CPU times of CP and ROM simulations [23].

There are two aspects to the significant advantage of the reduced order model over crystal plasticity. First, consider model parameter reduction. As stated at the end of Section 4.2, the ROM essentially involves 29 independent parameters, twenty (20) of which were treated as free in model identification. While this number may appear as large, it is a significant reduction in comparison with the *actual* independent parameters of crystal plasticity.

In a high-fidelity crystal plasticity formulation, the number of parameters scales with the number n of deformation systems (n = 30 for Mg, counting all variants). To each system are associated at least two strain-rate parameters, an initial

11

strength and n-1 hardening parameters in the interaction matrix. This leads to $\sim n(n+2) \approx 960$ parameters. Obviously, no crystal plasticity simulation would utilize the full extent of its inherent parameterization. But this already illustrates that conventional crystal plasticity is overly parameterized. In other words, the common usage of CP tacitly employs an ad hoc, and rather drastic, reduction in parameters. Typically, the number of parameters is reduced by taking many of them to be independent of slip/twin system (e.g. the strainrate parameters) or adopting functional forms for hardening that simplify the interaction matrix. In doing so, the formulation in Selvarajou et al. [12] for instance ends up with 26 parameters out of a possible 960.

Clearly, the huge reduction in putative model parameters is not the reason for computational gain when comparing the present ROM with CP for the numbers of free parameters are comparable (20 for the ROM versus 26 for CP). Besides, the number of parameters is only relevant for model identification.

The computational efficiency of the ROM over crystal plasticity simply resides in the reduction of the number of internal variables: two (2) for the ROM (p^g , p^t) versus thirty (30) for CP (all the slip/twin rates). In addition, the memory requirements to store the internal state variables are less with the ROM.

6.2. Representation of physical mechanisms

Kondori et al. [9] discussed some limitations of the reduced order model in capturing certain aspects of crystal plasticity. First, the ROM does not account for the twinninginduced material reorientation. Second, the ROM cannot describe mesoscale deformation features, such as texture evolution. Furthermore, the hardening laws used do not account for detwinning, which is believed to have a lower (effective) critical resolved shear stress. This effect could be incorporated using a back-stress formulation (kinematic hardening). This may have an additional contribution to the tension-compression asymmetry as well as in any unloading process. However, in Kondori et al. [9] the model was shown to capture the orientation dependence of the stress-strain response in three principal and three off-axes directions, including through the thickness of the plate, for which experimental data is scarce. The model also captured the evolution of tension-compression asymmetry and of plastic anisotropy in the form of 3D Lankford coefficients.

The present investigation goes one step further in probing the capabilities of the two-surface ROM to capture the essential features of crystal plasticity simulations. The competition between void-induced hardening and void-growth-induced softening is captured well. In addition, the ROM captures the formation of regions of tension and compressive states around the void through the stress differential parameter. Overall, the matching of both stress–strain and

porosity-strain responses is remarkable, especially for c-axis loading.

The strain levels reached in the voided cells are larger than one would expect for a specimen-level strain to failure in a Mg alloy, even when dimpled fracture is the main mechanism, e.g. Kondori and Benzerga [24,25]. However, that large strains may be reached locally is not excluded. To make further contact with experiments, one would need multi-void simulations or employ homogenized failure models. Another important aspect is that shear failure may occur in actual specimens. The role of plastic anisotropy in this regard is not well understood; see e.g. [26]. Here too, single-void simulations cannot reproduce that failure mechanism.

6.3. Parameter optimization strategy

Even for a simple anisotropic model such as Hill's [27], it is impossible to identify all parameters without, say uniaxial loading data along principal (L, T, S) and off-axes (LT, LS, TS) directions. Now, the reduced order plasticity model requires even more data to calibrate the anisotropic coefficients of glide, twin, and the stress asymmetry factor. Evidently, the datasets for a single crystal were incomplete, and only uniaxial tension data under prismatic and c-axis loading directions on the pristine single crystal were available. Therefore, we chose parameters reported by Kondori et al. [9] as the initial condition. We further improved the initial conditions of the 20 parameters by using CP simulations of a Mg polycrystal in various loading directions; see Appendix A. This pre-optimization step provided some estimates for the shear anisotropy coefficients that were left unperturbed by the c-axis or prismatic pristine material data.

One aim was to identify the parameters of the ROM using minimal data sets from Selvarajou et al. [12]. Several strategies have been attempted to achieve this:

• Strategy 1:

The ROM parameters are identified using uniaxial tension data on pure Mg along the prismatic and c-axis directions (Nos. 1 and 2 in Table 1). In this case, the uniaxial responses were calibrated better than shown in Fig. 3. However, predictions of unit cell results (Nos. 3–10 in Table 1) were far from satisfactory. For example, the strain to failure in the T=1 prismatic loading case was underestimated by 25% relative error. Also, under c-axis loading, the maximum flow stress was underestimated by over 20%.

• Strategy 2:

The ROM parameters are identified using only unit cell data for T=1 and the prismatic direction (No. 4 in Table 1). This strategy improves the anisotropic coefficients, particularly the shear coefficients, as the cell model has regions of shear stress states around the void. Hence, it delivers a better estimate for pristine and cell model cases compared to strategy 1. But, the quantitative comparisons under c-axis loading for the cell model still underestimated by at least 20%.

• Strategy 3:

12

The ROM parameters are identified using pristine material and cell data for T=1 along the prismatic direction (Nos. 1, 2, 4 in Table 1). This strategy minimizes the cost function even further. However, the ROM still fails to capture void-induced hardening, the flow stress level, and the strain to failure under c-axis loading. Hence, at least one unit cell data under c-axis loading is necessary.

Strategy 4:

The ROM parameters are identified using uniaxial tension data sets on pristine and cell model along the prismatic and c-axis directions (Nos. 1, 2, 3, 7 in Table 1). This strategy captures the void induced hardening, and hence the flow stress levels at all triaxialities under prismatic and c-axis loadings. However, the ROM overestimates the strain to failure in comparison with CP simulations. Thus, at least one triaxial tension data on cell model under prismatic and c-axis directions are judged to be necessary for the optimization process.

• Strategy 5:

The ROM parameters are identified using pristine material and cell model data for T=1 along both prismatic and c-axis directions (Nos. 1, 2, 4, 8 in Table 1). This is the strategy retained in Section 5.

Of course, using all available data would improve the predictions, but that does not help in understanding the predictive capabilities of the ROM and computational cost as it would take more iterations to converge.

There are two quantitative aspects that could be improved (i) the secondary hardening observed under prismatic loading at sufficiently low triaxiality (dashed curves in Fig. 7); and (ii) the transverse anisotropy of void growth, again for prismatic loading (see Fig. 8(b) and (c)). The former could be remedied by introducing a second Voce law in glide hardening, Eq. (12). The latter can be captured with the model as is. It would only require that the optimization process be carried out using full 3D unit cells.

On the computational side, some responses exhibited oscillations. The solver embedded in the UMAT is a simple Newton solver. Hence, the solution oscillates or overshoots for multiple systems and sometimes requires too fine a time step for convergence. Using trust region solvers or coupling Newton's iterative solver with line search techniques would reduce the computational time even further.

7. Conclusions

A reduced-order two-surface plasticity model was investigated by comparison against crystal plasticity simulations of voided and pristine unit cells.

 Although the calibration procedure uses only stress-train data, the constitutive model was found to capture the orientation-dependence of porosity evolution and the macroscopic response at all levels of stress triaxiality that were investigated.

- 2. The well-known effect of triaxiality was observed. The higher the triaxiality the lower the strain to coalescence. Void closure under uniaxial loading was also captured for *c*-axis loading.
- 3. The ROM captures the competition between void-induced hardening and porosity-induced softening. It captures the void-induced hardening through the activation of twinning or glide locally around the void due to regions of tension and compressive states.
- 4. Two drawbacks of the ROM were identified under prismatic loadings: the transverse anisotropy of void growth and the secondary hardening at low triaxiality. Both can be remedied in principle.
- 5. The reduced order plasticity model is highly efficient for computation. The memory needed to store internal state variables is cheaper. The model constitutes therefore a good basis to build upon for developing predictive models of damage accumulation to failure, especially in the context of high-throughput analyses for usage in machine learning methodologies.

Declaration of Competing Interest

Authors declare that they have no conflict of interest.

Acknowledgment

The authors gratefully acknowledge support of this work by the National Science Foundation (CMMI Award no. 1932975). We thank Prof. Shailendra Joshi from the University of Houston for supplying unit cell crystal plasticity simulation datasets.

Appendix A. Initial parameter set

To better calibrate the anisotropic shear coefficients and strength asymmetry factor, uniaxial tension and compression data in various directions are needed. Since the available data for single crystal Mg was incomplete, the initial conditions of the 20 parameters entered into the optimizer were obtained from a ROM calibration process using *polycrystal* Mg simulation data.

The data is taken from Indurkar et al. [20]. These authors generated tension stress-strain responses of pure Mg *polycrystal* data under L, T, S, LT, LS, and TS directions and uniaxial compression under L direction. Thus, the first optimization procedure involves minimizing the difference between the ROM and CP responses of pure Mg *polycrystal* data to identify initial parameters for further calibration. The calibration results are presented in Figs. 9 and 10. The results also show the capability of the ROM to capture responses in multiple loading directions. The trends captured by the ROM agree well with the CP results with high computational efficiency as ROM calibration is performed using a single finite element.

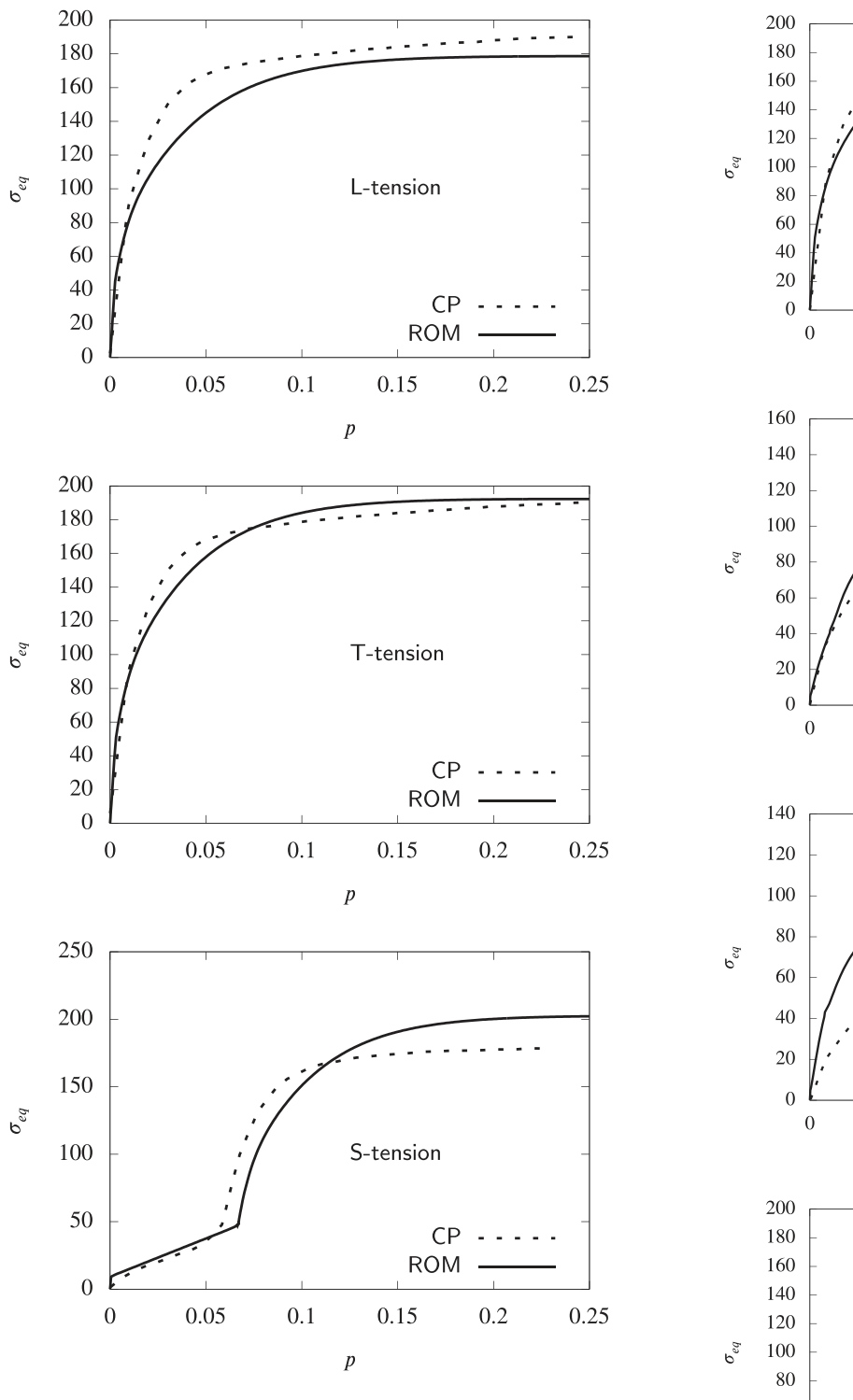


Fig. 9. Best fit of the ROM on crystal plasticity (CP) simulations in Indurkar et al. [20] for multiple loading orientations. Effective stress, $\sigma_{\rm eq}$, versus effective strain, p, for uniaxial tension along L,T,S directions of the polycrystal.

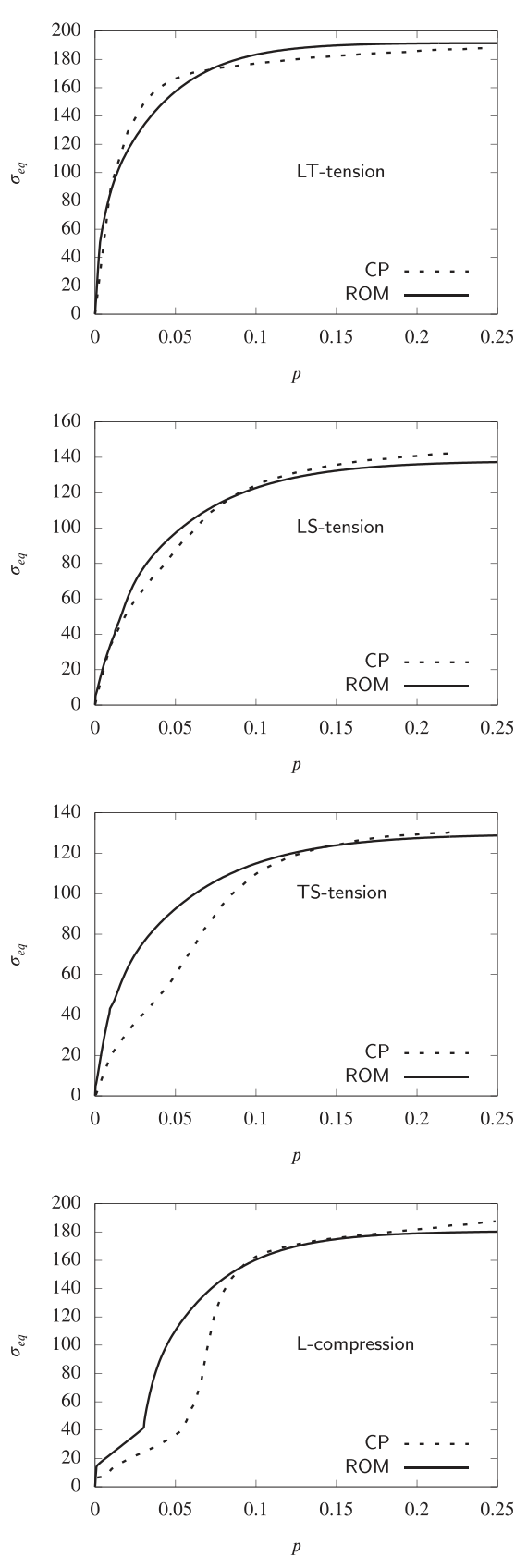


Fig. 10. Best fit of the ROM on crystal plasticity (CP) simulations in Indurkar et al. [20] for multiple loading orientations. Effective stress, $\sigma_{\rm eq}$, versus effective strain, p, for uniaxial tension along LT,LS,TS directions, and uniaxial compression along L direction of the polycrystal.

ARTICLE IN PRESS [m5+;May 30, 2023;11:24]

R. Vigneshwaran and A.A. Benzerga/Journal of Magnesium and Alloys xxx (xxxx) xxx

References

14

- [1] S.R. Kalidindi, J. Mech. Phys. Solids 46 (2) (1998) 267–290.
- [2] J. Zhang, S.P. Joshi, J. Mech. Phys. Solids 60 (5) (2012) 945–972.
- [3] Y. Chang, D.M. Kochmann, Int. J. Plast. 73 (2015) 39-61.
- [4] R.A. Lebensohn, C. Tomé, Acta Metall. Mater. 41 (9) (1993) 2611–2624.
- [5] S. Agnew, D. Brown, C. Tomé, Acta Mater. 54 (18) (2006) 4841–4852.
- [6] O. Cazacu, B. Plunkett, F. Barlat, Int. J. Plast. 22 (7) (2006) 1171-1194.
- [7] R. Becker, J. Lloyd, Mech. Mater. 98 (2016) 98-110.
- [8] D. Steglich, X. Tian, J. Besson, Eur. J. Mech. A/Solids 55 (2016) 289–303.
- [9] B. Kondori, Y. Madi, J. Besson, A. Benzerga, Int. J. Plast. 117 (2019) 71–92.
- [10] J.C. Michel, P. Suquet, J. Mech. Phys. Solids 90 (2016) 254–285.
- [11] R. Vigneshwaran, A. Benzerga, in: Magnesium Technology 2022, Springer, 2022, pp. 293–297.
- [12] B. Selvarajou, S.P. Joshi, A.A. Benzerga, J. Mech. Phys. Solids 125 (2019) 198–224.
- [13] P.P. Indurkar, S.P. Joshi, A.A. Benzerga, J. Mech. Phys. Solids (2022) 104923.

- [14] A.A. Benzerga, J. Besson, Eur. J. Mech. A/Solids 20 (3) (2001) 397–434.
- [15] F. Barlat, D.J. Lege, J.C. Brem, Int. J. Plast. 7 (7) (1991) 693-712.
- [16] Y. Zhu, M.D. Engelhardt, R. Kiran, Eng. Fract. Mech. 199 (2018) 410–437.
- [17] J. Koplik, A. Needleman, Int. J. Solids Struct. 24 (8) (1988) 835–853.
- [18] S.M. Keralavarma, S. Hoelscher, A.A. Benzerga, Int. J. Solids Struct. 48 (2011) 1696–1710.
- [19] Z-set/ZeBuLoN, 9.1.3. software package by ecole des mines paristech (France) and onera-the french aerospace lab. http://www.zset-software. com.
- [20] P.P. Indurkar, S. Baweja, R. Perez, S.P. Joshi, Int. J. Plast. 132 (2020) 102762.
- [21] A.A. Benzerga, J. Mech. Phys. Solids 50 (6) (2002) 1331-1362.
- [22] A. Pineau, A.A. Benzerga, T. Pardoen, Acta Mater. 107 (2016) 424–483.
- [23] S.P. Joshi, Private communication, 2022.
- [24] B. Kondori, A.A. Benzerga, Exp. Mech. 54 (2014) 493–499.
- [25] B. Kondori, A.A. Benzerga, Acta Mater. 124 (2017) 225-236.
- [26] A.A. Benzerga, N. Thomas, J.S. Herrington, Sci. Rep. 9 (2019) 1425.
- [27] R. Hill, Proc. R. Soc. Lond. Ser. A 193 (1033) (1948) 281-297.